

1 Performance of an acoustic sensing array in 2 a high-flow tidal channel

3 Matthew Auvinen, David Barclay

4 Abstract

5 Baseline ambient sound level assessment is important in quantifying additional noise contributions from tidal
6 energy infrastructure. Static acoustic sensing in high-flow conditions is complicated by pseudo-sound, or flow noise,
7 generated by pressure fluctuations due to turbulent flow on the surface of a hydrophone. Signal processing methods
8 are used to identify and suppress flow noise at low frequencies on a four-element horizontal hydrophone array with
9 data collected in the Minas Passage in October, 2016. Observations of spectral slope and spatial coherence are
10 used to track the masking effect of turbulence across frequency and flow speed, and identify the critical frequency
11 threshold where flow noise exceeds the ambient noise. The array's performance in the Minas passage is quantified
12 by an empirical relationship between current speed and the critical frequency. Beamforming and coherent averages
13 are proposed as possible flow noise suppression methods and evaluated.

14 Index Terms

15 Flow noise, ambient noise, acoustical array, tidal channel, and passive acoustic monitoring.

16 I. INTRODUCTION

17 **T**IDAL power utilities are currently leasing seafloor space within the Minas Passage with aspirations
18 of converting the energy of the region's tidal currents into electricity, a trend that has been supported
19 by favorable projections of the Passage's tidal energy capacity [1]. As these companies seek sector devel-
20 opment, it is important that they maintain sustainable industry practices. This includes the consideration
21 of industry knowledge gaps, many of which are a consequence of the industry's immaturity [2]. The

Matthew Auvinen is a former honours student of David Barclay's in the Department of Oceanography, Dalhousie University, Halifax NS, B3H4R2 Canada (email:matthewauvinen@gmail.com; DBarclay@Dal.Ca).

Manuscript received July XX, 2017; revised MONTX XX, 201X. This work was supported by GeoSpectrum, Black Rock Tidal Power, and the National Sciences and Engineering Research Council of Canada

22 uncertainty surrounding the ecological and environmental implications of tidal turbine infrastructure is a
23 particularly important industry knowledge gap and has qualified some opposition to turbine projects.

24 Tidal turbines present two serious environmental threats: physical contact (or interaction) and acoustic
25 pollution.

26 Large-scale tidal turbine sites could pose physical risks to boats, swimmers, marine mammals, and fishes
27 within tidal channels. The risk of turbine-human interaction can be mitigated with appropriate signage and
28 conspicuous warnings. However, the prevention of physical contact between animals and tidal turbines is
29 more challenging, and, in consequence, tidal turbines could seriously threaten local animals and regional
30 ecosystem health [3] [4].

31 Tidal turbines could become an important source of ambient noise in tidal channels through a variety
32 of mechanisms, such as motor or mechanical noise and cavitation [5]. Depending on the frequency and
33 levels of turbine noise, turbine anthropophony could affect animal navigation, communication, predator-
34 prey detections [6], and life cycles [7]. Moreover, turbine-generated sound could be damaging to fish
35 tissue [8]. These acoustic effects threaten near-field and far-field ecosystem health, stressing the need for
36 rigorous environmental impact assessments in the tidal power sector.

37 As such, tidal power companies are interested in establishing baseline ambient noise measurements
38 in the Minas Passage, against which turbine noise pollution will be measured. However, the utility of
39 ambient sensing is limited by pseudo-sound, or flow noise, generated on the surface of a hydrophone
40 in turbulent water. Indeed, the masking effects of flow noise can complicate source identification and
41 background noise assessment in high-flow settings, such as tidal channels.

42 Analogous to the turbulent air flow pseudo-sound described in [9], flowing water in a high Reynolds
43 number regime generates pressure fluctuations on the surface of a hydrophone. These pressure fluctuations
44 produce flow noise which is irregular, uncorrelated, and random. Local pressure fluctuations on the surface
45 of a hydrophone represent near-field turbulence [10]. Hydrophones moving with the mean water flow will
46 experience little signal contamination, as it is the *relative* flow of water over a hydrophone's surface that
47 leads to flow noise.

48 Turbulent flows occupy a wide range of frequencies and wavenumber domains, with broad spatial and
49 temporal variability. The advective nonlinearity of turbulent flows makes them unpredictable in space and
50 time, and contributes to their complex nature [11]. Despite being governed by classical mechanics and
51 cascade laws, turbulence and its corresponding flow noise are difficult to predict.

52 The degree of variability within turbulence (and flow noise) makes it difficult to reliably predict flow
53 noise characteristics. [6] identifies steep spectral slopes in a high-flow setting, an artifact of small-scale
54 turbulence averaged out across the surface of a submerged sensor. This steep spectral slope, f^{-m} , is
55 modeled and described in [12]. Furthermore, a spectral slope of $f^{-5/3}$ - not to be confused with the
56 coincidental wind-generated spectral slope, which occurs at higher frequencies [13] - has been reported
57 at frequencies below 10 Hz.

58 Flow noise presents a unique challenge for passive acoustic monitoring: a hydrophone in a high-flow
59 setting will record both propagating sound and pseudo-sound. This suggests that models should distinguish
60 between the two sound sources in order to properly evaluate ambient signals. [14] details a coherence-based
61 signal processing approach to flow noise suppression.

62 Successful suppression of flow noise could benefit passive acoustic monitoring (PAM) systems in the
63 tidal energy sector. Additionally, improved ambient sensing in high-flow conditions would enhance our
64 understanding of underwater ambient sound fields. The objectives of the present research are:

- 65 1) Use spectral analysis and spatial coherence to identify and characterize flow noise at low frequencies
66 (< 500 Hz).
- 67 2) Use beamforming and coherent averaging to improve the performance of a linear hydrophone array
68 by suppressing flow noise and enhancing the measurement of ambient noise.

69 This paper is organized as follows. Section II discusses important field work details, including site
70 description and instrumentation. Section III contains all relevant signal processing, including spectral
71 analysis, spatial coherence, and beamforming. Section IV presents the results of signal processing and
72 data analysis and Section V evaluates the results and identifies areas for future work. Lastly, Section VI
73 summarizes the findings of the study in a series of conclusions.

74 II. FIELD WORK

75 A. Site Description

76 The Bay of Fundy is characterized by a large tidal range, with amplitudes up to 18 meters at the head
77 of the Bay and 6 meters in the Minas Basin, an inlet connected to the rest of the Bay through the Minas
78 Passage. Field work was completed on October 27, 2016, near the Fundy Ocean Research Center for
79 Energy (FORCE) site in the Minas Passage of the Bay of Fundy. The deployment period spanned roughly
80 four hours, from 12:00 ADT to 16:00 ADT. This experimental window captured the transition from ebb
81 tide to slack tide.

82 Wind speed was measured intermittently throughout the deployment period using a hand-held wind
 83 speed gauge (Table I) and tidal data was generated using the WebTide models.

TABLE I
 WIND SPEED MEASUREMENTS TAKEN OVER THE DEPLOYMENT PERIOD.

Time (ADT)	Wind speed (m/s)
13:35	4.9
14:35	5.2
15:00	6.2
15:10	6.2
15:35	4.2
15:48	3.2

84 *B. Experiment*

85 A linear hydrophone array was towed from the *MV Nova Endeavour* (42' x 16'), which was anchored
 86 to the seafloor in the Minas Passage. The array was positioned 15 meters below the sea surface using a
 87 depressor and sampled four channels simultaneously over a 4 hour period. Array signals were transferred
 88 to the *MV Nova Endeavour* using a signal cable and processed by an analog-to-digital converter (ADC).
 89 The signal cable was attached to a tow cable (6GA galvanized wire) using cable ties, and carried both
 90 the array and a drogue. The signal cable was sheathed in a fairing to reduce strum generation.

91 A drifting hydrophone (guard buoy) was deployed using a small auxiliary vessel launched from the
 92 *MV Nova Endeavour*. The guard buoy was suspended at a depth of \sim 1 meter using a drifting float and
 93 isolation system made of spectra and compliant bungee. The system isolated the recording hydrophone
 94 and instrument package from any surface action, such as the vertical movement of waves, which would
 95 otherwise generate instrument or flow noise.

96 A total of five transects were performed by driving the guard buoy upstream, deploying the drifter,
 97 then floating downstream in a rigid-hulled inflatable boat (RHIB) alongside the guard buoy until \sim 50
 98 feet past the array. These transects were performed over the course of three hours, beginning at 13:00
 99 ADT. The guard buoy signals were (ideally) flow noise free and were used as benchmarks to assess the
 100 performance of the array.

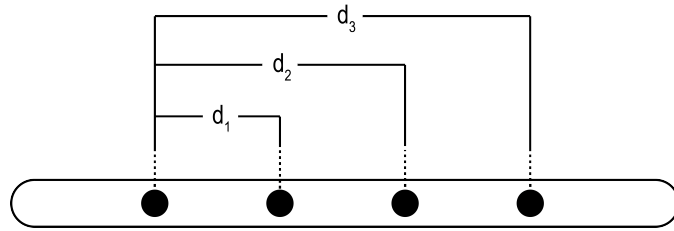


Fig. 1. Schematic view of linear array. Hydrophones are shown, as well as the corresponding separation distances. d_1 is 17cm, d_2 is 34cm, and d_3 is 51cm. Pair separation, d , is 17cm.

101 C. Instrumentation

102 The linear array was constructed by GeoSpectrum, and contains 4 sequentially spaced hydrophones
 103 with a horizontal configuration (Figure 1). Each hydrophone pair is separated by a distance of 17cm, d .
 104 The array hydrophones were set to sample at a rate of 96.038 kHz with an acoustic bandwidth of 48.019
 105 kHz. The four channels on the array continuously recorded 10 minute WAV files over a 4 hour period.
 106 The array elements recorded signals in units of counts. As such, power spectra were calibrated to dB re 1
 107 μ Pa according to frequency-dependent sensitivities. The guard buoy sampled at a rate of 96 kHz with an
 108 acoustic bandwidth of 48 kHz, and was equipped with a GPS to record transect geospatial information.
 109 The guard buoy is 79 centimeters in length and 14 centimeters in diameter. The guard buoy recorded
 110 WAV files in 30 minute segments and saved them to its 512 GB hard drive. The guard buoy records raw
 111 signals in units of counts, and corresponding power spectra were converted to dB re 1 μ Pa according to
 112 frequency-dependent sensitivities.

113 III. DATA ANALYSIS

114 Data analysis was performed in MATLAB in several stages. The analysis began with the calculation of
 115 the power spectral density (PSD) from the raw WAV files, followed by spectral analysis, spatial coherence,
 116 and beamforming. Visual assessment of the signal processing results provided direction for flow noise
 117 identification and characterization. Furthermore, quantitative evaluation of the results facilitated further
 118 description of the flow and ambient noise recorded during the deployment period.

119 A. General Signal Processing

The output of a hydrophone is defined as

$$x_i(t) = \sigma_i(t) + n_i(t) \quad (1)$$

120 where x_i is the recorded time series on each i th hydrophone, σ_i is the sound field's ambient components,
 121 and n_i is the locally generated flow noise. Importantly, n_i and σ_i are uncorrelated. Furthermore, the
 122 inherent randomness of flow noise makes n_i incoherent with respect to n_j .

The power spectrum, or spectral density, is defined as

$$S_{ii}(\omega) = \frac{\langle X_i(\omega) \cdot X_i^*(\omega) \rangle}{T} \quad (2)$$

123 where X_i is the Fourier transform of x_i , ω is angular frequency, $*$ denotes a complex conjugate, $\langle \rangle$
 124 indicates an ensemble average, and T is the observation interval. All Fourier transforms are windowed
 125 by a Hann function. The Fourier transform is 2^{16} points long and contains 99 degrees of freedom.

Coherence is used to quantify the similarity between two signals. Here, coherence is defined as

$$\Gamma_{ij}(\omega) = \frac{S_{ij}(\omega)}{(S_{ii}(\omega) \cdot S_{jj}(\omega))^{\frac{1}{2}}} \quad (3)$$

126 B. Power Spectrum Probability Density

127 Spectral probability density (SPD) is an analytical technique used to depict the variability of the power
 128 spectrum over a period that is much longer than the minimum time required for a stationary measurement
 129 of power to be made [15]. This form of analysis facilitates the identification of unique events within a
 130 series of spectra.

The power spectrum probability density (PSPD) is defined as

$$\text{PSPD}(f) = H(S_{ii}(f), h) \quad (4)$$

131 where $\text{PSPD}(f)$ is the power spectrum probability density at frequency f , and $H(S(f), h)$ is the histogram
 132 of the power spectrum S_{ii} at frequency f with a histogram bin width of h dB re 1 μPa . By combining
 133 PSPD results across frequencies, we generate a PSPD matrix

$$\begin{bmatrix} \text{PSPD}(f_1) & \text{PSPD}(f_2) & \text{PSPD}(f_3) & \dots & \text{PSPD}(f_a) \end{bmatrix} \quad (5)$$

134 where $\text{PSPD}(f_a)$ is the PSPD at the a th frequency.

135 C. Spectral Critical Frequency

136 [6] and [12] suggest that there are three distinct spectral slope regions in the low-to-mid-frequency
 137 range: at < 10 Hz, spectra follow Kolmogorov's $f^{-5/3}$ spectral slope; at $10 < f < 100$ Hz, spectral

138 slopes correspond to f^{-m} due to small-scale turbulence flow noise interacting with the finite size of the
 139 sensor surface [12]; at $f > \sim 100$ Hz, spectral slopes are determined by near-field and far-field ambient
 140 sound sources.

Any given spectral slope is defined as

$$f^{-M} = \frac{S_{ii}(2\pi f_a) - S_{ii}(2\pi f_b)}{\log(f_a \cdot f_b^{-1})} \quad (6)$$

141 where $S_{ii}(2\pi f_a)$ is the spectral density on the i th sensor at frequency f_a and $S_{ii}(2\pi f_b)$ is the spectral
 142 density on the i th sensor at frequency f_b . Equation 6 describes the spectral slope in dB/decade. f^{-m} from
 143 [12] is found using Equation 6 between 10 Hz and 40 Hz ($a = 10$ Hz, $b = 40$ Hz).

The transition from the flow noise region of f^{-m} to the ambient noise region is marked by the ‘frequency knee’, where the spectral slope begins to shallow. That is, the exit from the flow noise region is marked by a deviation below the slope f^{-m} . Here, critical frequency, f_c , is defined as the first frequency at which

$$|f^{-M}| < |f^{-m}| \quad (7)$$

144 is true. Importantly, both slopes in Equation 7 are in dB/decade. This form of analysis produces the
 145 ‘spectral critical frequency’, f_c .

146 D. Coherence Critical Frequency

147 Spatial coherence is calculated for each channel combination using Equation 3, providing an assessment
 148 of signal similarity between elements. Propagating ambient noise is highly correlated across the array.
 149 Additionally, propagating noise at wavelengths sufficiently large relative to element spacing produces very
 150 high coherence at low frequencies by effectively co-locating sensors. Conversely, flow noise is a source
 151 of incoherence, as pseudo-sound is uncorrelated across the linear array (when turbulent scales are lesser
 152 than hydrophone separation). Therefore, in the band $f < 500$ Hz, flow noise is marked by low coherence
 153 while ambient noise is marked by high coherence. The transit of this coherence boundary, from flow noise
 154 (incoherent) to ambient noise (coherent) provides a metric for describing the extent of flow noise across
 155 the array.

156 The spatial coherence critical frequency, f'_c , is defined as the frequency at which a minimum coherence
 157 threshold is crossed. Record length, hydrophone spacing, and other physical details suggest a reasonable
 158 spatial coherence threshold range of 0.7 - 0.9.

Formally, f'_c is the first frequency at which

$$|\Gamma_{ij}(\omega)| \geq G_{ij} \quad (8)$$

is true. Here, G_{ij} is the empirical spatial coherence threshold, unique for each hydrophone pair. This spatial coherence threshold method facilitates the identification of the ‘coherence critical frequency’.

161 E. Linear Regression

162 A linear regression between critical frequencies, f_c and f'_c , and flow speed, u , is used to identify and
 163 characterize the prevalence of flow noise and ambient noise in measurements. Importantly, no data points
 164 are excluded from this regression.

165 F. Beamforming

We use a broadside beamformer to coherently average the channels across the array. Ideally, this process suppresses stochastic values and enhances correlated terms. Locally generated flow noise and the ambient sound field are inseparable, however we can describe their relative prevalence with the theoretical signal-noise ratio (SNR). By taking the Fourier transform of Equation 1 and substituting into Equation 2, we find

$$S_{ii} = \frac{\langle X_i(\omega) \cdot X_i^*(\omega) \rangle}{T} \quad (9)$$

$$S_{ii} = \frac{\langle (\varsigma_i + N_i) \cdot (\varsigma_i^* + N_i^*) \rangle}{T} \quad (10)$$

where ς_i and N_i are the Fourier transforms of σ_i and n_i , respectively. For clarity, the frequency dependency has been omitted. Since ς_i and N_i are uncorrelated, we can expand Equation 10 to arrive at

$$S_{ii} = \frac{\langle \varsigma_i \varsigma_i^* \rangle + \langle N_i N_i^* \rangle}{T} \quad (11)$$

Given Equation 11, the SNR for a single hydrophone (SNR_H) is defined as

$$\text{SNR}_H = \frac{\langle \varsigma_i \varsigma_i^* \rangle}{\langle N_i N_i^* \rangle} \quad (12)$$

where $\text{SNR}_H = 1$ at the critical frequency, f_c . Now consider an array of hydrophones indexed by i , where the ambient sound field component of the signal on each phone is

$$\sigma_{i+1}(t) = \sigma_1(t - \tau_i) \quad (13)$$

where

$$\tau_i = \frac{i \cdot d \cos \theta}{c} \quad (14)$$

is the acoustic travel time in seconds, for plane wave noise arriving on the sensors at the angle θ . Here, d is the nearest neighbour element separation (Figure 1). Taking the Fourier transform of Equation 13 gives

$$\varsigma_i(\omega) = \varsigma_1(\omega) e^{-i\omega\tau_i}. \quad (15)$$

The coherent sum of the signals on each element, with no time delay, is defined as

$$x_T(t) = \sum_{i=1}^l x_i(t) \quad (16)$$

where $x_i(t)$ is the signal recorded on the i th element of a linear array l elements long. $x_T(t)$ is the equivalent to beamforming broadside to the array. Since the source of interest is ambient noise, the sound field is assumed to be axially symmetric. Thus the horizontal array orientation and beam direction are unimportant, provided an appropriate array gain compensation is applied. The Fourier transform of Equation 16 is

$$X_T(\omega) = \sum_{i=1}^l X_i(\omega). \quad (17)$$

The array power spectral density can be estimated using Equation 17 by

$$A = \frac{\langle X_T(\omega) \cdot X_T^*(\omega) \rangle}{T}. \quad (18)$$

Given an array with both ambient noise and flow noise components, Equation 17 can be expanded to

$$X_T = [\varsigma_1 + N_1 + \varsigma_2 + N_2 + \dots + \varsigma_l + N_l] \quad (19)$$

which describes the total output of all sensors on an array with l elements. Substituting Equation 15 into Equation 19 gives

$$X_T = \varsigma_1 + N_1 + \sum_{i=1}^l (\varsigma_1 e^{-i\omega\tau_i} + N_{i+1}). \quad (20)$$

Using the Fourier transform of the coherently summed outputs across the array, the power spectral density can be computed by substituting Equation 20 into Equation 18 yielding

$$A = \frac{\langle \varsigma_1 \varsigma_1^* \left[l + \sum_{i=1}^{l-1} \frac{1}{2} (l-i) \cos(\omega\tau_i) \right] + N \cdot N^* \rangle}{T} \quad (21)$$

where

$$N = \sum_i^l N_i \quad (22)$$

is the coherently summed flow noise. This term can be simplified by assuming the power of the flow noise measured on each individual hydrophone is equal across the array,

$$\langle N_i N_i^* \rangle = \langle N_j N_j^* \rangle \quad (23)$$

and uncorrelated between the sensors,

$$\langle N_i N_j^* \rangle = \delta_{ij} \cdot N_1 N_1^* \quad (24)$$

166

$$\delta_{ij} = \begin{cases} 0 & \text{if } i \neq j \\ 1 & \text{if } i = j. \end{cases}$$

Then the total power received by the array becomes

$$A = \frac{\langle \varsigma_1 \varsigma_1^* \rangle \left[l + \sum_{i=1}^{l-1} \frac{1}{2} (l-i) \cos(\omega\tau_i) \right] + l \langle N_1 N_1^* \rangle}{T} \quad (25)$$

Futhermore, if K is defined as

$$K = l + \sum_{i=1}^{l-1} \frac{1}{2} (l-i) \cos(\omega\tau_i) \quad (26)$$

then Equation 25 becomes

$$A = \frac{K\langle \zeta_1 \zeta_1^* \rangle + l\langle N_1 N_1^* \rangle}{T} \quad (27)$$

where Equation 27 describes the array spectral density. Here, SNR_A describes the prevalence of the ambient noise and flow noise components of the array output, such that

$$SNR_A = \frac{K\langle \zeta_1 \zeta_1^* \rangle}{l\langle N_1 N_1^* \rangle} \quad (28)$$

Comparing Equation 28 to the result derived for a single hydrophone, given by Equation 12, we see that the beamformed array improves the signal-to-noise ratio by a factor of $\frac{K}{l}$. Furthermore, Equation 28 suggests that array performance improves with an increasing number of hydrophones, l . For an array with 4 elements, at broadside, $\frac{K}{l} = \frac{7}{4}$.

171 G. Array Gain

The broadside beamforming analysis applied to the linear array generates artificial spectral density gain. As a result, an array gain formula is applied to the beamformed results to correct the inflated values. The array gain formula presented here is adapted from [16], such that

$$AG = 20 \log l \quad (29)$$

The array gain correction is performed by subtracting the result of Equation 29 from the calculated array power spectral density.

174 H. Algorithm Assessment

Equations 17 and 18 can be used to consolidate all channel signals into one array signal. Spectral slope analysis of the array spectral density, A , using Equations 6 and 7 ascertains the prevalence of flow noise across the beamformed array. The resulting critical frequencies of the coherent array can be compared to the spectral and coherence critical frequencies of a single hydrophone to critically evaluate the performance of the beamformed array.

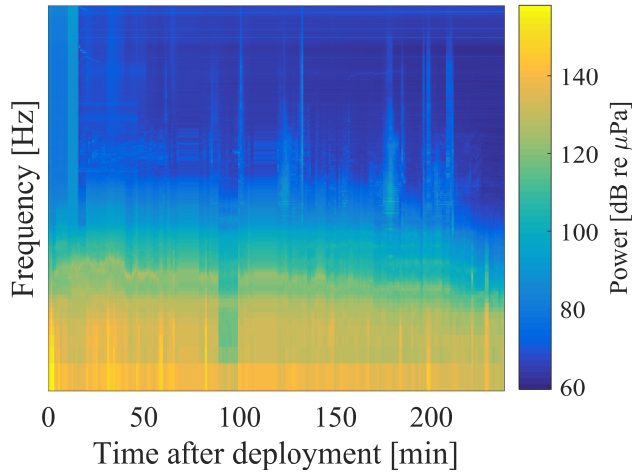


Fig. 2. Power spectrum for channel 0 on the array. The spectrum is plotted over the deployment period across a range of low-to-mid frequencies. The spectrum begins at maximum ebb tide and ends at slack tide. Power decreases with flow speed over the deployment period.

IV. RESULTS

181 A. Spectral Density

182 Signal levels (Figure 2) are relatively high in fast flowing water and low in slow flowing water. The
 183 mid-to-high-frequency band is less affected by flow noise and is quiet relative to lower frequencies (i.e.
 184 < 10 Hz), where there is a substantial amount of flow noise.

185 The hydrophone power spectrum contains multiple episodes of mid-frequency noise. These signals are
 186 attributed to ship noise generated by the small vessel used in the guard buoy drifter tests. Additionally,
 187 the abrupt shift in spectral densities at ~ 90 minutes is due to equipment reconfigurations.

188 B. Power Spectrum Probability Density

189 The PSPD facilitates the broad-scale assessment of a hydrophone's spectral density over entire deploy-
 190 ment periods. The PSPD for channel 0 is shown in Figure 3.

191 The PSPD follows a spectral slope of $f^{-5/3}$ below 10 Hz, behaviour analogous to Kolmogorov's
 192 turbulence theory. This spectral slope marks a region of flow noise within the signal. A steepened spectral
 193 slope of f^{-m} , where $m > \frac{5}{3}$, persists between 10 to 100 Hz, a result of small-scale turbulence when
 194 turbulence wavelength \ll sensor size. This small-scale turbulence is averaged out over the surface of
 195 the hydrophone sensor, dampening the measured signals. The PSPD results show that ambient noise is
 196 dominant above 300 Hz, where signal levels are markedly low. There is an electronic system noise floor
 197 present at about 60 dB re μPa .

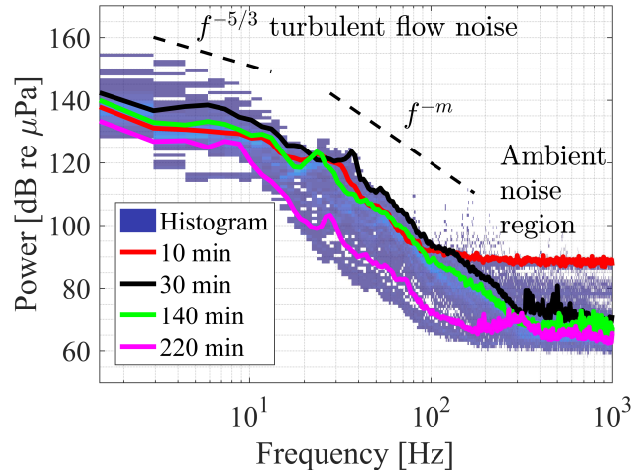


Fig. 3. Channel 0 power spectrum probability density over the entire deployment period. Turbulent flow noise is prevalent < 10 Hz (where wavelengths \gg sensor size), with a spectral slope of $f^{-5/3}$, while turbulent flow noise interacting with a hydrophone's finite size (in the 10 Hz to 100 Hz band) yields a spectral slope of f^{-m} . The ambient sound field dominates at ~ 300 Hz. Time indicates the signal snapshot time stamp.

198 Signal snapshots are superimposed on the PSPD and suggest that measurements in slow current con-
199 ditions contain a greater extent of ambient noise relative to those in fast current conditions.

200 *C. Spectral Critical Frequency*

201 Equation 6 was used to iteratively calculate the spectral slope between 10 and 100 Hz. The linear
202 relationship between spectral slope, f^{-m} , and current, u , (Figure 4) indicates that signals recorded in
203 decreasing flow are increasingly damped. The spectral slopes observed between 10 and 100 Hz range
204 from -25 to -60 dB/decade.

205 The critical frequency was iteratively calculated over the experimental period using Equation 7. The
206 critical frequencies were regressed against current, as shown in Figure 5. There is a positive correlation
207 between critical frequency and current speed, where fast flow coincides with high spectral critical fre-
208 quencies. The spectral critical frequency is used to track the transition from the flow noise region to the
209 ambient noise region.

210 Importantly, the intercepts have not been forced to zero. This is because it is unrealistic to expect that
211 we can completely eliminate flow noise, or low-frequency noise generated by the mechanical systems that
212 comprise the tow body. If this were a moored system with no surface expression, that assumption might
213 be valid, but is not considered here.

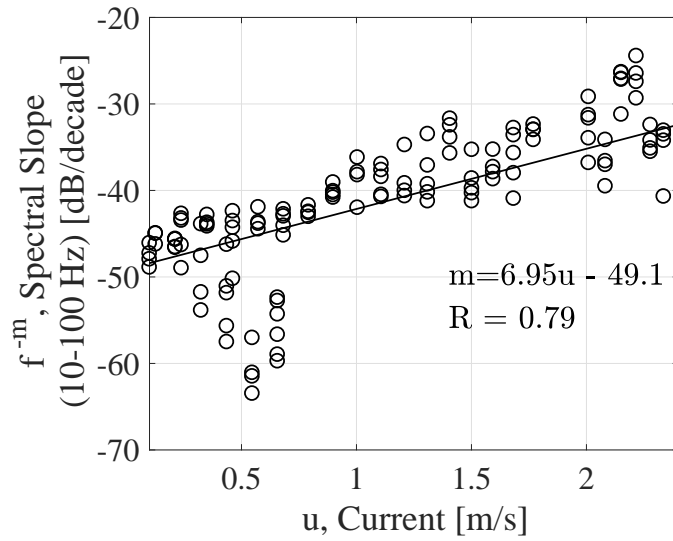


Fig. 4. Current speed dependence on flow noise spectral slopes, m , for channel 0. Spectral slope magnitude increases with decreasing flow. Spectral slope magnitudes remain greater than Knudsen's theoretical -17 dB./decade. Spectral slopes, f^{-m} , are between 10 and 100 Hz. Correlation coefficients, R , are reported.

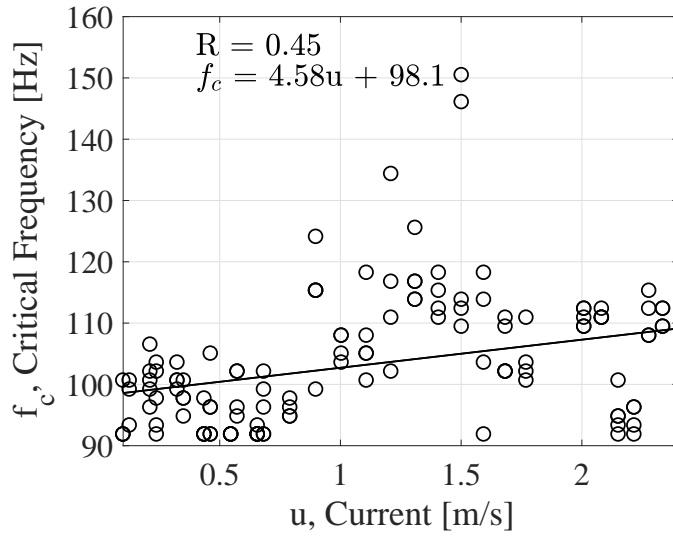


Fig. 5. Current speed dependence of critical frequency, f_c , as defined in equation 7. Critical frequency reveals where flow noise is no longer dominant. Correlation coefficients, R , are reported.

214 D. Spatial Coherence

215 Spatial coherence is calculated for different hydrophone combinations across the linear array using
 216 Equation 3. The spatial coherence results are presented in magnitude coherence for the entire deployment
 217 period (Figure 6). If the wavelength of propagating sound is sufficiently long the sensors would become
 218 relatively co-located. However, the results suggest that the low frequency data is overwhelmingly inco-
 219 herent. This implies that uncorrelated flow noise is eroding this wavelength-coherence relationship, since
 220 the locally generated flow noise is incoherent across the array.

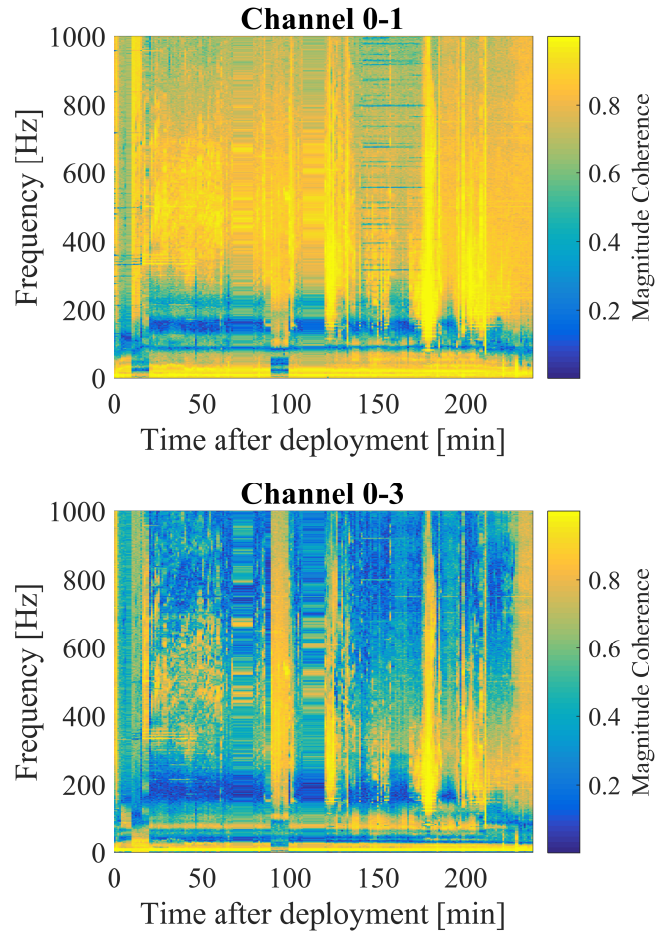


Fig. 6. Channel spatial coherence over the experimental period. Magnitude coherence is expected to tend to unity as the hydrophones become relatively co-located. However, uncorrelated flow noise on each phone breaks that relationship. Incoherent flow noise regions decrease as current speed slows.

221 Flow noise is uncorrelated and propagating ambient noise is highly correlated at low frequencies (relative
 222 to hydrophone spacing). As a result, low coherence and high coherence are a sign of flow noise and ambient
 223 noise, respectively. Therefore, the spatial coherence results are partitioned into two distinct regions: a flow
 224 noise region and an ambient noise region. Visual assessment suggests that flow noise is consistently present
 225 at low frequencies and can be prominent at higher frequencies (above 600 Hz) if hydrophone separation
 226 distance is sufficient. The ambient noise region is present between 200 and 600 Hz and contains the same
 227 vessel noise identified in Figure 2.

228 *E. Coherence Critical Frequency*

229 The coherence critical frequency is the frequency at which the boundary between the ambient noise and
 230 flow noise regions occurs. The coherence critical frequency was iteratively calculated for each combination

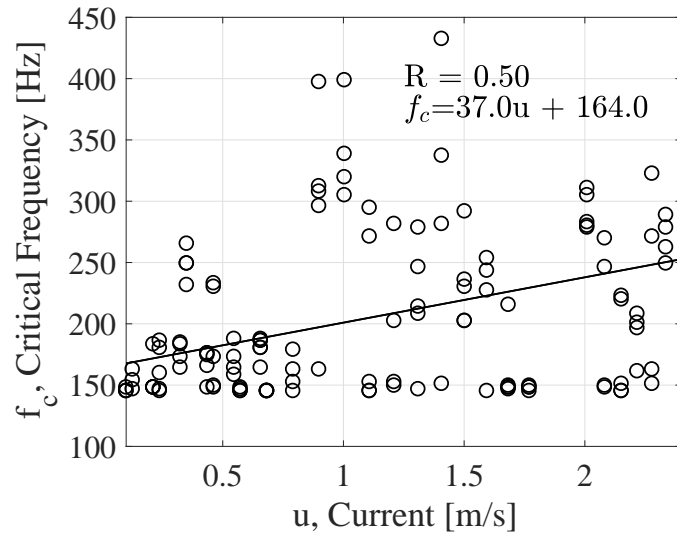


Fig. 7. Current dependency of spatial coherence threshold. Spatial coherence threshold used to detect the critical frequency in a more precise way than the spectral sloping method.

of channels, and is used to quantify the relative prevalence of flow noise and ambient noise within a measurement (Figure 7). The coherence critical frequency is a more rigorous method of flow noise measurement than the spectral critical frequency, as spatial coherence is an indicator of flow noise *cessation* rather than noise region *transition*. The coherence critical frequency increases with increasing flow speed, a relationship similar to that of the spectral critical frequency.

It is important to note that the coherence is impacted by any temporary deterministic noises present in the sound field, such as the auxiliary RHIB, mechanical array noise, or noise generated aboard the Nova Endeavour. In such instances, the automated critical frequency detector fails, and yields an outlier.

There is a good deal of noise in Figure 7, as no outliers nor oddities were discarded. The retention of outliers is done to maintain the integrity of the linear regression. This makes the regression statistically rigorous and suggests that the correlation is meaningful.

242 F. Beamforming

The spectral critical frequencies of the beamformed array can be compared to the spectral and coherence critical frequencies of the single hydrophone, as shown in Figure 8. The shaded sections around each critical frequency regression shows one standard deviation of each critical frequency method. The standard deviations of the spectral slope and spatial coherence critical frequency regressions were extracted from the averaged fits, while the standard deviation of the coherent array critical frequency regression was calculated from the data during the regression.

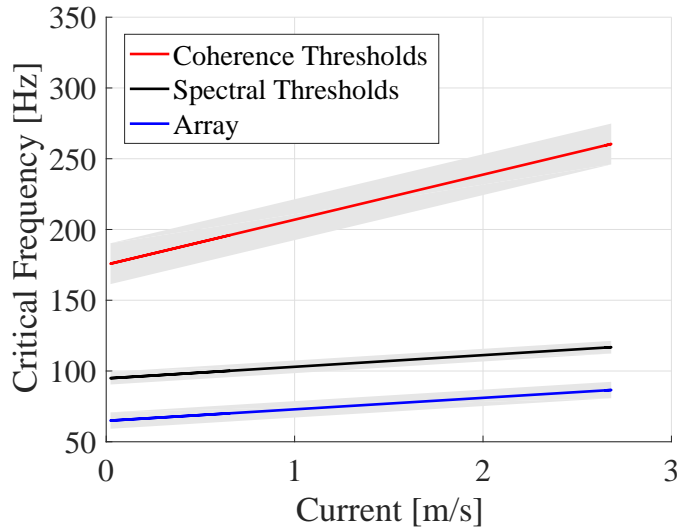


Fig. 8. Comparison of hydrophone spectral slope, coherence threshold, and array spectral slope critical frequency identification methods. Coherence and spectral analysis reveal regions of flow, ambient, and mixed noise. Uncertainties are 1 standard deviation (shaded).

249 The coherence critical frequency identification method yields a relatively high threshold, while spectral
 250 critical frequencies (both single hydrophone and beamformed array) are relatively low. This is attributed
 251 to the rigorous and precise nature of the coherence-based method. Above coherence critical frequencies
 252 we can be confident that there is no contamination of the ambient noise field by flow noise. Conversely,
 253 the single hydrophone and coherent array thresholds show where the dominant noise transitions from flow
 254 noise to ambient noise. The critical frequency regressions serve as upper and lower bounds of different
 255 noise regimes. Importantly, the coherent array contains significantly lower critical frequencies than the
 256 single hydrophone, indicating that the broadside beamforming approach lessens the extent of flow noise
 257 on the measurements.

258 Figure 9 compares guard buoy, single hydrophone, and coherent array power spectra at 1.5 hours into
 259 the experiment. The spectra are selected based on the drifter's distance from the *MV Nova Endeavour*
 260 and the timestamps of each transect. We select a time where the drifter and array were in close proximity
 261 to establish a meaningful comparison.

262 The guard buoy spectrum behaves differently from the rest, exhibiting significantly lower levels at
 263 frequencies below 100 Hz. A frequency shoulder, or pronounced excursion in spectral slope, is present
 264 at 10 Hz in the guard buoy spectrum, suggesting non-negligible flow noise is affecting the guard buoy
 265 measurements. This is typical of all moored or free drifting passive acoustic systems that have a surface
 266 expressions or subsurface float. The single hydrophone shows clear symptoms of flow noise at low
 267 frequencies.

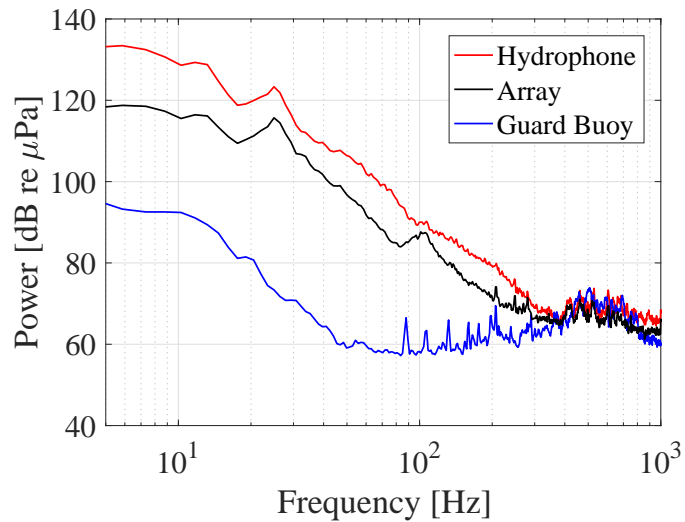


Fig. 9. Comparison of hydrophone, coherent array, and guard buoy signals captured at 1.5 hr into the deployment.

The spectra reveal that the coherent array spectra transitions to the ambient noise region at lower frequencies than the single hydrophone (excluding the guard buoy). Furthermore, the array signals are quieter than the single hydrophone signals at low frequencies. There is reasonable agreement between the guard buoy and coherent array above the critical frequency, with some difference above 700 Hz. This disparity is attributed to the lack of co-location between the array and the guard buoy, as they are vertically and horizontally displaced relative to each other. Coherent averaging across the array does not seem to jeopardize signal variability.

V. DISCUSSION

A. Spectral Critical Frequency

Results show that critical frequency and flow speed are positively related, indicating that flow noise is increasingly prevalent in fast current conditions. This is intuitive, as flow noise and current speed are intimately related. The spectral slope critical frequency presents a new method of identifying the transition between flow noise and ambient noise dominance. As such, the spectral slope critical frequency results could lead to improvements in flow noise models.

The nature of spectral critical frequencies provides two important insights. Firstly, frequencies above the critical frequency will contain a mixture of ambient noise and flow noise, since the threshold merely marks the *reduction* in flow noise, and not the *absence*. Secondly, frequencies below the critical frequency will exclusively contain flow noise, since the spectral slopes align with turbulence theory. These insights

286 are important, as they provide useful context for future signal level and sound-source evaluations in tidal
287 channel measurements.

288 *B. Spatial Coherence*

289 Spatial coherence results for different sensor combinations show that there are two distinct coherence
290 regions across the array: an incoherent flow noise region and a coherent ambient noise region. The
291 prevalence of these regions is quantified with the coherence critical frequency. Iterative calculations of the
292 coherence critical frequency were regressed against current speed. There is a positive relationship between
293 coherence critical frequency and current speed, similar to the spectral critical frequencies. The coherence
294 critical frequency facilitates the identification of the cessation of flow noise within a signal.

295 These results are linked to the spectral sloping critical frequencies such that the spectral critical
296 frequency provides a lower boundary, below which only flow noise exists, and the coherence critical
297 frequency method provides an upper boundary, above which only ambient noise exists. Intermediate
298 frequencies contain a mixture of flow noise and ambient noise. This explains why the coherence critical
299 frequencies are noticeably higher than those of the spectral sloping method. The application of spectral
300 and coherence critical frequencies provides valuable insight on the relative extent of both ambient noise
301 and flow noise within a signal.

302 *C. Beamforming*

303 By effectively treating the array as one sensor or hydrophone, signal processing can address the pseudo-
304 sound within low frequency data. Coherent averaging suppresses flow noise and enhances the detection of
305 propagating ambient noise. The coherent averaging employs a broadside approach with no steering angle,
306 and is outlined in Equation 18.

307 The results of the beamformed array are shown in Figure 8. Evidently, the coherent array contains
308 lower levels and lower critical frequencies than the single hydrophone (Figure 9). This implies that the
309 coherent array is less affected by flow noise, and contains a greater extent of ambient noise.

310 VI. CONCLUSION

311 Flow noise appears in two regions: as $f^{-5/3}$ noise when wavelength \gg sensor size, and as f^{-m} , where
312 the sensor's finite dimension reduces the flow noise at relatively higher frequencies. f^{-m} is related to the

313 flow speed over the array. A spectrum's deviation from f^{-m} slope indicates where flow noise is no longer
 314 dominant. Spatial coherence can be used to identify when effect of flow noise is negligible.

315 Coherent processing (beamforming) suppresses flow noise and yields a lower spectral critical frequency
 316 at all flow speeds than that of a single hydrophone. An increased number of hydrophones and array length
 317 could improve array performance, allowing passive acoustic monitoring at arbitrarily low frequencies.

318

REFERENCES

- 319 [1] R. Karsten, A. Swan, and J. Culina, "Assessment of arrays of in-stream tidal turbines in the bay of fundy," *Phil. Trans. R. Soc. A*, vol.
 320 371, no. 1985, p. 20120189, 2013.
- 321 [2] R. Inger, M. J. Attrill, S. Bearhop, A. C. Broderick, W. James Grecian, D. J. Hodgson, C. Mills, E. Sheehan, S. C. Votier, M. J. Witt
 322 *et al.*, "Marine renewable energy: potential benefits to biodiversity? an urgent call for research," *Journal of Applied Ecology*, vol. 46,
 323 no. 6, pp. 1145–1153, 2009.
- 324 [3] M. J. Dadswell, "Occurrence and migration of fishes in minas passage and their potential for tidal turbine interaction," 2010.
- 325 [4] A. Redden and M. Stokesbury, "Acoustic tracking of fish movements in the minas passage and force demonstration area: Pre-turbine
 326 baseline studies (2011-2013)."
- 327 [5] D. Wang, M. Atlar, and R. Sampson, "An experimental investigation on cavitation, noise, and slipstream characteristics of ocean stream
 328 turbines," *Proceedings of the Institution of Mechanical Engineers, Part A: Journal of Power and Energy*, vol. 221, no. 2, pp. 219–231,
 329 2007.
- 330 [6] A. Lombardi, "Soundscape characterization in grand passage, nova scotia, a planned in-stream tidal energy site," 2016.
- 331 [7] M. K. Pine, A. G. Jeffs, and C. A. Radford, "Turbine sound may influence the metamorphosis behaviour of estuarine crab megalopae,"
 332 *PLoS One*, vol. 7, no. 12, p. e51790, 2012.
- 333 [8] M. Halvorsen, T. Carlson, and A. Copping, "Effects of tidal turbine noise on fish," *PNNL Report-20787 for US Dept of Energy*, WA,
 334 DC: by Pacific Northwest National Laboratory, Sequim, WA, pp. 1–41, 2011.
- 335 [9] M. Lighthill, "The bakerian lecture, 1961. sound generated aerodynamically," in *Proceedings of the Royal Society of London A: Mathematical, Physical and Engineering Sciences*, vol. 267, no. 1329. The Royal Society, 1962, pp. 147–182.
- 336 [10] M. Strasberg, "Nonacoustic noise interference in measurements of infrasonic ambient noise," *The Journal of the Acoustical Society of America*, vol. 66, no. 5, pp. 1487–1493, 1979.
- 337 [11] M. Van Dyke, *An album of fluid motion*. Parabolic Press Stanford, 1982, vol. 176.
- 338 [12] C. Bassett, J. Thomson, P. H. Dahl, and B. Polagye, "Flow-noise and turbulence in two tidal channels," *The Journal of the Acoustical Society of America*, vol. 135, no. 4, pp. 1764–1774, 2014.
- 339 [13] V. O. Knudsen, R. Alford, and J. Emling, "Underwater ambient noise," *J. Mar. Res.*, vol. 7, pp. 410–429, 1948.
- 340 [14] D. R. Barclay and M. J. Buckingham, "Depth dependence of wind-driven, broadband ambient noise in the philippine sea," *The Journal
 341 of the Acoustical Society of America*, vol. 133, no. 1, pp. 62–71, 2013.
- 342 [15] N. D. Merchant, T. R. Barton, P. M. Thompson, E. Pirotta, D. T. Dakin, and J. Dorocicz, "Spectral probability density as a tool for
 343 ambient noise analysis," *The Journal of the Acoustical Society of America*, vol. 133, no. 4, pp. EL262–EL267, 2013.
- 344 [16] H. Cox, "Line array performance when the signal coherence is spatially dependent," *The Journal of the Acoustical Society of America*,
 345 vol. 54, no. 6, pp. 1743–1746, 1973.

349

Michael Shell Biography text here.

PLACE

PHOTO

HERE

350

351

John Doe Biography text here.

352

Jane Doe Biography text here.